Proceedings of 20th International Congress on Acoustics, ICA 2010

23-27 August 2010, Sydney, Australia

Prediction of surface particle velocity from above-ground sound sources

Keith Attenborough (1), Shahram Taherzadeh (1) and Donald Albert (2)

(1) Department of Design, Development, Environment and Materials, The Open University, Milton Keynes, MK76AA, UK
(2) US Army ERDC CCREL, Hanover, NH 03755-1290 , USA

PACS: 43.20.Gp, 43.28.Js

ABSTRACT

The porous structure and near-surface layering of ground influences propagation of acoustic and seismic pulses originating from above-surface sound sources. Snow cover modifies the acoustical properties and frozen ground adds to the layering effect. A numerical model, Pulse Fast Field Program for Layered Air Ground Systems (PFFLAGS), developed originally (as FFLAGS) for continuous sound sources, is outlined. It is used to fit radial and vertical seismic signals recorded by a geophone and resulting from above-ground explosions over three types of ground including 'hard' and 'soft' soil and snow cover. An effective linear source pulse has been determined assuming that non-linear effects are small at the ranges of interest. The resulting deduction of parameters describing the near-surface ground structure is based first on fitting pore-related parameters to the above-ground acoustic waveforms received by microphones and then fitting the other parameters including elastic constants and layer dimensions to the vertical and radial components of soil velocity measured by collocated geophones. A similar procedure involving conjunctive use of buried probe microphone and geophone data has been used for fitting acoustic-to-seismic coupling spectra for quarry sand and a dry friable soil. Prospects for using this approach more generally for deducing soil strength, air permeability, moisture content and structure from non-invasive acoustic and seismic measurements are discussed.

INTRODUCTION

When an explosive charge is detonated above or on the surface of the ground, a pressure wave begins to propagate away from the charge location. As this pressure wave propagates over and interacts with the ground surface, it induces ground vibrations i.e. an air-coupled seismic wave. In addition to the ground vibrations induced during propagation along the ground surface, the airblast also interacts with the ground directly beneath the source producing waves that propagate as seismic waves within the ground. Since these waves travel mainly in high speed layers, they result in precursor seismic signals that arrive before the main acoustically-coupled arrival. Because these waves are small compared to the air-coupled waves, they have not been extensively studied. On the other hand they carry additional information about the ground layer structure.

There are several applications concerned with deducing information about a source from the resulting seismic disturbances. For example low frequency seismic stations detect and provide information about natural atmospheric phenomena including meteoroids and thunder. Sonic booms from aircraft, rockets, and space vehicle reentry are studied also using seismic sensors. The phenomenon of acoustic-to-seismic coupling is relevant to these and other sensing systems. Indeed sensor systems using geophones to detect air or ground vehicles can be greatly influenced by ground conditions.

On the other hand, if the acoustic signals are supplied from a known source, they can be used to give information about the medium over which or into which they propagate using methods similar to those used in Non Destructive Evaluation. For example, acoustically-induced ground vibrations have been used to locate buried landmines. Another relatively unexplored application is the non-invasive determination of soil strength and structure. Current methods for assessing soil structure are based on the inspection of a pit dug by hand. The only current *in-situ* method for determing soil strength requires a series of spot measurements with a penetrometer. This measures the mechanical resistance of the soil to a probe and is, therefore, invasive as well as laborious.

This paper outlines a model for predicting seismic disturbances from above-ground explosions or continuous sound sources and explores the extent to which it has enabled fitting to geophone signals measured in soils, sand and snow. Ways in which experience from such use of the model could lead to a procedure for non-invasive determination of soil strength and structure are discussed.

MODELLING GROUND AS A LAYERED POROELASTIC MATERIAL

Soils may be regarded as partially-saturated porous media. The acoustical properties of fluid-saturated homogeneous porous media have been studied widely in various contexts. Models for these properties make use of parameters related to the frame elasticity and the pores. A widely-employed model [1] predicts two kinds of coupled compressional waves, sometimes called Type I and II waves, and a shear wave. The Type I and shear waves travel mainly through the solid matrix and involve interactions between particles. They are equivalent to the P- and S- waves induced by direct mechanical excitation, for example during a seismic refraction survey. The Type II wave travels mainly through the fluid-filled pores being attenuated by viscous friction and thermal exchanges. It is dominant during acoustic excitation, i.e. from sound sources above an unsaturated soil surface, since the primary path for sound into the soil is through the pores connected to the surface. The interaction of above- and underground waves can be addressed by considering an inhomogenous system composed of vertically stratified homogenous medium composed from air and soil layers. The key modelling tool for this is the **F**ast **F**ield program for **L**ayered **A**ir-**G**round **S**ystems (FFLAGS) [2] which is analogous to the Fast Field Programs used for predicting underwater and outdoor sound propagation. It assumes horizontal stratification of the ground and allows for three wave types in each layer. Two of these correspond to the 'standard' P- and S- waves used in geophysical analysis, which travel mainly in the solid particulate framework of the soil. The third wave type is a 'slow' compressional wave travelling mainly through the pore structure [1]. The Green function method, a Hankel transform and numerical integration are used to solve for the magnitudes and phases of reflected and transmitted waves at each interface due to any number of (continuous) sound sources above or within the layered system.

Biot [3, 4] developed a theory of propagation of waves in a porous elastic medium by considering stresses and strains on fluid and solid components. Assuming a potential energy *W* Biot wrote stress-strain relations in terms of derivatives of *W*. Through introduction of the kinetic energy, *T*, and the Lagrange's equations for the aggregate, the equations of coupled motion for the propagation of waves were derived. Viscous effects were included by adding a viscosity correction function to the equations to compensate for the breakdown of Poiseulle flow in the pores. Biot's equations of motion in two-phase media, as modified by Stoll [5], assuming time-harmonic potentials, are:

$$\nabla^2\left(\overline{H}\phi_s - \overline{C}\phi_f\right) = -\omega^2\left(\rho\phi_s - \rho_f\phi_f\right), \tag{1}$$

$$\nabla^2\left(\overline{C}\phi_s - \overline{M}\phi_f\right) = -\omega^2\left(\rho_f\phi_s - \rho'\phi_f\right) \tag{2}$$

where ρ' can be considered as a complex fluid density:

$$\rho' = m - \frac{i\eta}{\omega\kappa}F(\lambda) \tag{3}$$

and

$$m = q^2\rho_f / \Omega \tag{4}$$

is a factor that accounts for extra inertia due to the fact that not all fluid flows along the axis of pores. The symbols q^2 and Ω, represent tortuosity (related to the formation factor for electrical resistivity) and volume porosity of connected pores respectively. The symbols η and κ represent dynamic fluid viscosity and permeability respectively and ω is the angular frequency. The viscosity correction function, $F(\lambda)$, arises from the viscous drag of the fluid in the pores. It accounts for the breakdown of the Poiseuille flow in the pores and depends on a dimensionless parameter relating to the thickness of the boundary layer at the pore walls. In (3), $\eta F(\lambda)$ is a dynamic viscosity factor with

$$\lambda = \frac{1}{2s_p}\left(\frac{8\rho_0 q^2\omega}{\Omega\sigma}\right)^{1/2} = \left(\frac{2\rho_0 q^2\omega}{\Omega\sigma s_p^2}\right)^{1/2}$$

Here σ is the flow resistivity, with units of Pa s m^{-2} which represents the ratio of the applied pressure gradient within a porous material to the induced fluid volume velocity for steady flow. The parameter s_p is a dynamic pore shape factor (= 1 for cylindrical pores) [6] and tortuosity is calculated from $\Omega^{-n'}$ where n′ is a grain shape factor (= 0.5 for spherical grains). *H*, *C* and *M* are effective bulk moduli of elasticity. *H* can be thought of as the corresponding effective modulus of the solid, while *C* and *M* are moduli involving coupling with the entrained fluid. The three (complex) moduli are determined from the solid and fluid bulk moduli of the constituent parts [5]:

$$H = \left[\frac{(K_s - K_b)^2}{D - K_b} + K_b + \tfrac{4}{3}\mu\right], \tag{5}$$

$$C = K_s\frac{\left(K_s - K_b\right)}{D - K_b}, \tag{6}$$

and

$$M = \frac{K_s^2}{D - K_b} \tag{7}$$

where

K_s = Bulk modulus of the solid grains,
K_b = bulk modulus of the drained solid matrix,
K_f = bulk modulus of the pore fluid, and

$$D = K_s\left[1 + \Omega\left(\frac{K_s}{K_f} - 1\right)\right]. \tag{8}$$

In general, the fluid bulk modulus is influenced by the thermal drag experienced by the fluid in the pores and hence it is complex and frequency dependent. This is particularly important in air-filled pores.

The corresponding equations of motion for the rotational motion are:

$$\mu\nabla^2\chi_1 = -\omega^2\left(\rho\chi_1 - \rho_f\chi_2\right), \tag{9}$$

$$0 = \left(\rho_f\chi_1 - m\chi_2\right) - \frac{i\eta}{\kappa\omega}F(\lambda)\chi_2 \tag{10}$$

where μ is the rigidity modulus of the material.

Writing the vector potentials $\chi_{1,2}$ in terms of a scalar potential ϕ_3 and using cylindrical coordinates:

$$\tilde{\chi}_1 = -\frac{\partial\phi_3}{\partial r}\hat{\theta}, \tag{11}$$

$$\tilde{\chi}_2 = m_3\tilde{\chi}_1 \tag{12}$$

The fact that the fluid rotational motion is proportional to the solid rotational motion (eqn. (12)) means that it is coupled and not independent. This is the result of Biot's assumption that the fluid is an ideal fluid and does not support vorticity. The solid displacement (***u***) and relative fluid displacement (***w***) can be expressed in terms of the three potentials:

$$\tilde{u} = \nabla\phi_s + \nabla\times\chi_1, \tag{13}$$

$$\tilde{w} = \Omega(\tilde{u} - \tilde{U}) = \nabla\phi_f + m_3\nabla\times\chi_1 \tag{14}$$

Here, *U* is the absolute fluid displacement and *w* is the volume averaged relative fluid displacement.

Substitution of a plane wave potential in Biot's equations (1) and (2) and setting the coefficient determinant equal to zero, yields the following dispersion equation for the dilatational phase velocities:

$$\left(\rho_f^2 - \rho\rho'\right)v_i^4 + \left(\overline{H}\rho' + \rho\overline{M} - 2\rho_f\overline{C}\right)v_i^2 + \left(\overline{C}^2 - \overline{HM}\right) = 0 \tag{15}$$

where v_i $(=\omega/k_i)$ are the phase velocities.

Equation (15) has two roots. Frequently the two corresponding dilatational waves are called “fast” and “slow” waves. Both have components in the fluid and the solid. The “fast” wave travels chiefly in the solid with little attenuation. Usually it is faster than the other waves in soils (hence the name). It is very similar to the P-wave used in traditional seismic analysis. The “slow” wave, on the other hand, is a highly attenuated and dispersive wave with a low phase speed which travels mainly in the fluid. Biot points out that, in this wave, the solid and fluid are moving out of phase. Attenborough [6] has explored conditions under which the slow wave is similar to the ‘pore wave’ predicted in rigid porous media. At audio frequencies in high flow resistivity soils, it is diffusive in nature. There are, however, circumstances under which the slow wave also becomes a true propagating wave. This occurs at high porosity and high frequencies. If either K_b=0 (pure fluid) or K_f=0 (elastic limit) then (15) has only one solution and the corresponding dispersion equation for a fluid or an elastic medium is retrieved.

The shear wave speed can be determined from equations for the rotational motion in a similar fashion

$$v_3^2 = \frac{\mu\rho'}{\rho\rho' - \rho_f^2} = \frac{\mu}{\rho - \rho_f^2 / \rho'} \qquad (16)$$

The single shear wave predicted in the porous elastic solid is very similar to the S-wave in non-porous elastic media since the second term in the denominator is small.

In FFLAGS, each of two inhomogeneous media in contact (e.g. a fluid above a poro-elastic ground) is considered to consist of vertically stratified homogeneous layers. The system is assumed to be bounded from above by homogeneous fluid half-space and from below by a homogeneous solid half-space [2]. The wave equation in each layer, assuming a time dependence of exp(-$i\omega t$), is

$$\nabla^2 \Psi_i(r,z) + k_j^2 \Psi_i(r,z) = \delta_j(r,z) \qquad (17)$$

where Ψ_i are the scalar displacement potentials for various wave types propagating in the medium, k_j (=ω/c_j) are the corresponding wave numbers in layer j and δ_j represent source terms i.e. it is possible to consider multiple sources. One compressional wave propagates in the fluid. Two compressional waves and one shear wave may propagate in each porous elastic ground layer. The wave numbers for the ground waves are determined from the dispersion equations. Subscript i=0 is used to denote the fluid wave. Subscripts i=1,2 are used to denote the two compressional waves and i=3 is used for the shear wave in the solid layer. A cylindrical system of co-ordinates is employed throughout.

Noting that there is radial symmetry, it is possible to separate the radial and vertical variables and, thus, to convert the partial differential equation (17) to an ordinary differential equation. Hankel transform integral pairs are used to represent the potentials:

$$\Psi_i(r,z) = \int_0^\infty \psi_i(z,k_r) J_0(k_r r) k_r dk_r$$

and (18 a&b)

$$\psi_i(z,k_r) = \int_0^\infty \Psi_i(r,z) J_0(k_r r) r dr$$

where $J_0(z)$ is the zero order Bessel function and k_r, the variable of integration, can be thought of as the horizontal or radial component of the wave number. Applying the second of these to the wave equation yields the transformed Helmholtz Equation:

$$\frac{\partial^2}{\partial z^2}\psi_i + \beta_j^2 \psi_i = S_j \delta(z) \qquad (19)$$

where

$$\beta_j^2 = k_j^2 - k_r^2 \qquad (20)$$

and the right hand side is the source term. In this way the problem of determining the wave amplitudes is reduced to one of solving a set of ordinary differential equations (ODE's). The boundary condition equations (BCE’s) are put in the form of a Global Matrix equation

$$\mathbf{A} \cdot \mathbf{X} = \mathbf{B} \qquad (21)$$

where **X** is a vector containing the wave amplitudes(A_i in the porous medium and R_i in the fluid), **A** is an N×N matrix containing the coefficients from the BCE’s and **B** is the source term vector. The order of the matrix, N, is related to the number of fluid layers, n_f, and the number of solid layers, n_s, both including the half-space, by:

$$N = 6(n_s - 1) + 2n_f + 2 \qquad (22)$$

Equation (21) can be solved by a variety of methods including Gaussian elimination with pivoting.

Subsequently the forward Hankel transform is applied to obtain the full wave solutions. The essence of the FFP technique is that once the Green's functions (the range-independent ψ_i) are known as a function of k_i, the transform can be replaced by a Fast Fourier Transform. This may be calculated in the far field by substituting a large argument approximation for the Bessel function. The integral can then be evaluated very quickly and efficiently using Discrete Fourier transform techniques available in signal processing. The inherent limitation in this process is that $k_r r >> 1$ which restricts the model to ranges greater than a couple of wavelengths from the source. The solution in the first fluid layer may be expressed by:

$$\psi_0 = R^{\uparrow} e^{j(z-h1)\beta_0} + R^{\downarrow} e^{-j(z-h2)\beta_0}, \qquad (23)$$

where, *h1* and *h2* denote the vertical coordinates of the lower and upper fluid layer boundaries (*h2* > *h1*) and *z* is in the direction away from the fluid-solid interface.

Similarly for each poroelastic layer, there are three potentials given by

$$\psi_1 = A_1^{\downarrow} e^{j(z-d1)\beta_1} + A_1^{\uparrow} e^{-j(z-d2)\beta_1} + A_2^{\downarrow} e^{j(z-d1)\beta_2} + A_2^{\uparrow} e^{-j(z-d2)\beta_2} \qquad (24)$$

$$\psi_2 = m_1[A_1^{\downarrow} e^{j(z-d1)\beta_1} + A_1^{\uparrow} e^{-j(z-d2)\beta_1}] + m_2[A_2^{\downarrow} e^{j(z-d1)\beta_2} + A_2^{\uparrow} e^{-j(z-d2)\beta_2}] \qquad (25)$$

$$\psi_3 = A_3^{\downarrow} e^{j(z-d1)\beta_3} + A_3^{\uparrow} e^{-j(z-d2)\beta_3}, \qquad (26)$$

where, *d1* and *d2* denote the upper and lower solid boundaries (|*d2*| > |*d1*|) and z is positive downwards from the interface. $R^{\updownarrow}$ and $A_n^{\updownarrow}$ (*n = 1, 2, 3*) are the amplitudes to be determined from the boundary condition equations. Each potential consists of upgoing and downgoing terms. Also, because the two compressional wave types can exist simultaneously in solid and pore fluid phases, the potentials are a linear superposition of the two wave solutions with m_i being the appropriate ratios of solid-borne wave to pore-borne wave.

The boundary conditions involve the solid and fluid displacements and stresses. The fluid displacement is

$$\nabla \Psi_0 = \left(\frac{\partial \Psi_0}{\partial r}, \frac{\partial \Psi_0}{\partial z} \right) \qquad (27)$$

and the pressure is $\rho\omega^2\Psi_0$.

In the ground the solid phase displacement, u, is

$$\tilde{u} = \nabla \Psi_1 + \nabla \times \tilde{\chi}_1 \qquad (28)$$

The radial and vertical components of solid displacement are given by

$$u_r = \frac{\partial \Psi_1}{\partial r} + \frac{\partial^2 \Psi_3}{\partial r \partial z}, \qquad u_z = \frac{\partial \Psi_1}{\partial z} - \frac{1}{r}\frac{\partial}{\partial r}\left(r \frac{\partial \Psi_3}{\partial r} \right) \tag{29}$$

It is convenient to use the relative fluid motion and its components defined by

$$\tilde{w} = \nabla \Psi_2 + \nabla \times \tilde{\chi}_2 , \qquad w_r = \frac{\partial \Psi_2}{\partial r} + m_3 \frac{\partial^2 \Psi_3}{\partial r \partial z}, \qquad w_z = \frac{\partial \Psi_2}{\partial z} - m_3 \frac{1}{r}\frac{\partial}{\partial r}\left(r \frac{\partial \Psi_3}{\partial r} \right) \tag{30}$$

where, χ_i are vector potentials representing the transverse motion (see equations 21 and 22), and m_3 is the ratio of fluid rotational motion to the solid one.

To allow a time dependent acoustic source pulse $f_S(t)$ to be input to the continuous wave model [2], the source pulse is Fourier transformed in the time domain to obtain a pulse spectrum

$$F_s(\omega) = \frac{1}{\sqrt{2\pi}} \int_{t=0}^{\infty} e^{i\omega t} f_S(t) dt \tag{31}$$

The wave amplitude F at a point with cylindrical coordinates (r_m , z) due to a unit source at (0, z_0) for a given angular frequency ω is derived from Hankel transform of the one-dimensional solution of the wave equation, Γ:

$$F(r_m, z) = \frac{\Delta k \sqrt{N}}{2\pi \sqrt{m}} \left(e^{-i\pi/4} \sum_{n=0}^{N-1} \frac{\Gamma(k_n, z)}{\sqrt{n}} e^{2i\pi mn/N} + e^{i\pi/4} \sum_{n=0}^{N-1} \frac{\Gamma(k_n, z)}{\sqrt{n}} e^{-2i\pi mn/N} \right) \tag{32}$$

where N is the n index upper bound for the finite summation evaluating the Hankel's transform, m is the index for the range discretization, $r_m = m\Delta r = \frac{2\pi m}{N\Delta k}$, is the range, $\Delta k = \frac{k_{\max}}{N-1}$ is the horizontal wave number increment and $k_n = n\Delta k$. $\Gamma(k_n, z)$ is the product of k_n and the Green's function for the problem which is detailed elsewhere [2].

Equation (32) is based on a large argument approximation of Bessel function and the replacement of the integration by a finite sum over index n in the Hankel transform. Two Fast Fourier Transforms are used to evaluate the sums in equation (32). Correction factors (ε, η) are needed to allow for the truncation of the infinite integral associated with the Hankel transforms and for the presence of poles on the real axis. The integration contour is displaced by $\varepsilon\Delta k$ and a function $A(1-\exp(-\eta k_N))$ is subtracted from the integrand in the Hankel transform, where A can be expressed in terms of N, ε, η and the integrand. The values of the correction parameters ε and η used for the calculations reported here are 1.1 and $3/k_{max}$ where k_{max} is the upper limit of the integration.

In PFFLAGS, the predicted pulse spectrum is evaluated using Equations (31) and (32). The predicted time domain pulse follows from the inverse Fourier transform of the pulse spectrum as

$$\Psi_R(t) = \frac{1}{\sqrt{2\pi}} \int_{\omega=0}^{\infty} e^{-i\omega t} F_s(\omega) F(r_m, z, \omega) d\omega \tag{33}$$

PREDICTIONS AND DATA FOR EXPLOSIONS OVER 'HARD' AND 'SOFT' SOILS

Various charge sizes of C4, ranging from 1 to 128 blocks (0.57 to 73 kg) were detonated at a height of 1.5 m above ground level in an approximately 500 × 500 m field of sandy soil covered in light vegetation consisting of grass, weeds and a few scattered small trees [7]. The resulting signatures were measured using a digital seismograph for propagation distances of 10 to 240 m. At each sensor location, either a solid state PCB pressure sensor or a ¼ inch diameter Bruel and Kjaer microphone was used to record the air blast wave at the ground surface level. Since the solid state sensors were capable of measuring higher pressure levels they were generally usually used for propagation distances of 100 m and less, while the microphones were used at greater distances. These pressure sensors were calibrated in the field using a Trig-Tek Model 402H calibrator capable of producing a high pressure signal at 62.5 and 125 Hz. In addition, Mark Products L-15 geophones with a resonant frequency of 4.5 Hz were used to record the ground vibrations. The geophones included one vertical component, and either one (radial) or two (radial and transverse) horizontal components. The geophones produce a voltage output that is proportional to the ground particle velocity. The geophones have a flat response from 4.5 Hz to above 500 Hz but were not calibrated *in situ*

Geophones and collocated microphones were installed at 100, 120, 180, and 240 m from the source location. The soil at this site is subsequently called 'hard' soil. Another series of charges were detonated near the centre of an approximately 4 km × 1 km field covered in light vegetation including grass and weeds. Collocated geophones and microphones were at distances of between 60 m and 405 m from the source. Subsequently, the soil at this second site is called 'soft'.

Figure 1 shows the assumed source waveform based on measurements made close to C4 explosions but after adjusting the amplitude, assuming spherical spreading, to fit that of the acoustic waveform recorded at 100m on the 'hard' soil site (see Figure 2). This replaces the nonlinear source by an equivalent linear source. Nevertheless the nonlinear nature of the source signals is manifested by the high apparent speed of sound (358.5 m/s). Although the source waveform amplitude (Figure 1) was adjusted to give reasonable agreement with the 'hard' soil data at 100m (Figure 2(a)), it is used without further modification to obtain the parameters for fitting measured acoustic pulses over 'soft' soil (Figure 2(b)). The parameters used to obtain the predictions are listed in Table 1.

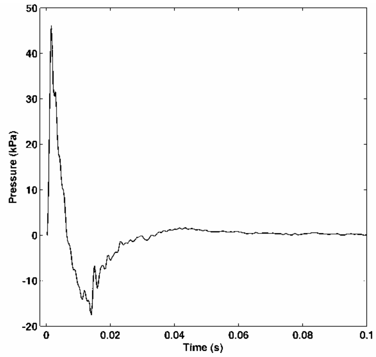

Source [7]

Figure 1. Source pulse waveform assumed for predictions based on measurements made close to C4 explosions but with the peak amplitude adjusted to give a good fit to the 'hard' soil acoustic data at 100m.

In the absence of seismic refraction information for the sites, a relatively simple structure of a single porous and elastic layer over a semi-infinite porous and elastic substrate has been assumed. However, even for this simple structure, the PFFLAGS code introduces seventeen unknown parameters.

The acoustic pulse predictions are influenced mainly by four pore-related parameters (σ, Ω, s_p, n') and are relatively insensitive to ground elasticity and layering. Consequently while fitting for the pore-related parameters, typical values of elasticity parameters and an upper layer thickness of 0.1 m or greater can be assumed. A relatively high value of flow resistivity and a relatively low porosity value are necessary to fit the acoustic pulse data above the 'hard' soil which is known to have been compacted. Conversely, the flow resistivity and porosity values required to fit the acoustic pulse above 'soft' soil are lower and higher respectively than the corresponding values for the 'hard' soil.

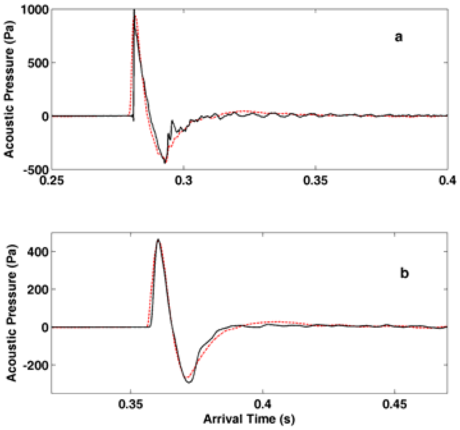

Source [7]

Figure 2. Measurements (continuous lines) and predictions (broken lines) of the acoustic pulse waveforms with microphone on the ground (a) over 'hard' soil 100m from the source and (b) over 'soft' soil 120m from the source. The parameters used for the predictions are listed in Table 1.

Table 1. Ground parameters used for predictions (Figs. 2-4)

	Parameter	Hard	Soft
Layer	flow resistivity (σ, kPa s m^{-2})	927	127
	Porosity (Ω)	0.17	0.37
	Pore shape factor (s_p)	0.3	0.3
	Grain shape factor (n')	0.5	0.5
	P-wave speed (ms^{-1})	600	490
	S-wave speed (ms^{-1})	400	290
	Soil density (ρ, kg m^{-3})	1700	1900
	Layer thickness (m)	1.5	2.7
	Wave attenuation constant (α)	0.02	0.02
Sub-strate	flow resistivity (σ, kPa s m^{-2})	1600	1600
	Porosity (Ω)	0.07	0.07
	Pore shape factor (s_p)	0.3	0.3
	Grain shape factor (n')	0.5	0.5
	P-wave speed (ms^{-1})	2040	2040
	S-wave speed (ms^{-1})	1120	1020
	Soil density (ρ, kg m^{-3})	2600	2600
	Wave attenuation constant (α)	0.05	0.05

Source: [7]

The P- and S- wave speeds and thickness of the upper porous and elastic layers have been determined by trial and error fitting of the seismic data; starting with typical values and having fixed the pore-related parameters at values that give good fits to the acoustic pulse data. The fitted values are listed in Table 1.

The seismic wave speeds (V_p = 600 m/s, V_s = 400 m/s) needed to fit the first arrivals in the measured 'hard' soil waveforms (Figure 3) are higher than those (V_p = 490 m/s, V_s = 290 m/s) that fit the measured 'soft' soil waveforms (Figure 4).

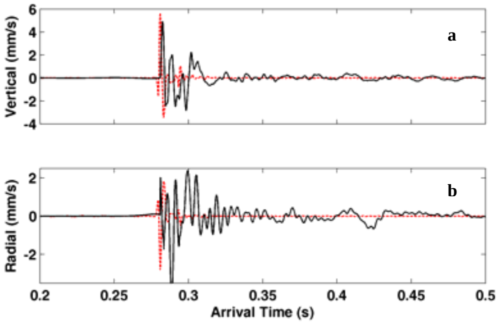

Source: [7]

Figure 3. Measured (continuous lines) and predicted (broken lines) waveforms of (a) soil vertical particle velocity and (b) soil radial particle velocity waveforms at a geophone buried at a depth of 1 cm in 'hard' soil 100 m from the source. The prominent late arrivals observed in the data for both vertical and radial seismic components are probably the result of multiple layers below the topsoil not included in the model. The parameters used for the predictions are listed in Table 1.

A consequence of the assumed simple structure (a single 1.5 m thick layer over a higher wave speed substrate) for the calculated seismic signals in 'hard' soil is that, although they require wave speeds such that $V_p > V_s > c$, they fail to predict the prominent peaks in the measured waveforms which are observed in the measured waveforms after the first arrivals. It is likely these are the result of a more complicated ground structure including more than two layers.

Even after assuming a simple two-layer structure, predictions of the seismic waveforms for the 'soft' soil (Figure 4), as well as suggesting a greater upper layer depth (2.7m), are able to reproduce the 'ringing' observed in both vertical and radial components. The values used for the predictions are such that $V_p > c > V_s$.

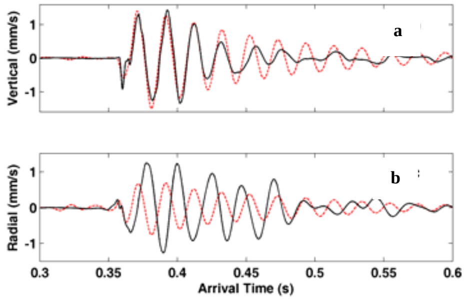

Source: [7]

Figure 4. Measured (continuous lines) and predicted (broken lines) waveforms of (a) soil vertical particle velocity and (b) soil radial particle velocity waveforms at a geophone buried at a depth of 1 cm in 'soft' soil located 120 m from the source. The parameters used for the predictions are listed in Table 1.

PREDICTIONS AND DATA FOR EXPLOSIONS OVER SNOW

Measurements have been made in a snow-covered area about 200 x 200 m in size, free of vegetation but with somewhat rough ground with high spatial variations on the order of 30-50 cm in height. The snow cover was very low density and low strength. Detonations were made of various charge sizes of C4, ranging from 0.5 to 8 blocks (0.28 to 4.5 kg) on the surface and at a height of 1.5 m above ground level and the resulting signatures were measured for propagation distances between 30 and 100 m. The snow cover was fairy shallow and weak, so the geophones were installed by drilling mounting holes into the frozen soil and freezing them in place. Thus, while a snow cover affected the acoustic wave propagation, the solid particle motion measured was in the frozen soil, rather than in the relatively weak, overlying snow layer. Snow characterization was carried out after the explosions by which time a considerable area near the charge location was clear of snow. The thickness of the snow cover ranged from 10 to 15 cm and it had an extremely low density of 60 – 90 kg m^{-3}. At several locations there was a thin crust with a higher density of 330 kg m^{-3}. Air permeability measurements were also conducted on small samples using a flow rig, yielding values of between 35 and 40 × 10^{-10} m^2. The measured permeabilities correspond to flow resistivities between 4.47 and 5.1 kPa s m^{-2}.

Figure 5 shows measured and predicted acoustic pulse waveforms at the snow surface 100 m from the explosion.

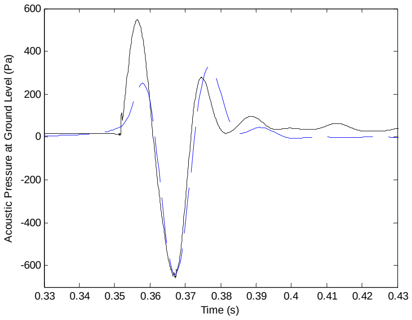

Source [7]

Figure 5. Measured (solid line) and predicted (broken line) acoustic pulse data at the snow surface 100m from the source. Parameters used for the predictions are in Table 2.

The best fit of the acoustic pulse data (Figure 5) is obtained by assuming that the snow has a thin surface layer (crust) consistent with the non-acoustically-measured density profile. The fitted total thickness of the snow layer (15 cm) corresponds to the greatest depth measured but the predictions are not very sensitive to the assumed thickness of the lower (2^{nd}) snow layer. The assumed flow resistivity of the snow layer beneath the crust is based on the snow core data in Table 2.

There are significant secondary arrivals and a minor precursor in the measured vertical seismic component. The observed secondary arrival in the vertical seismic component (Figure 6(b)) and the earliest precursor (Figure 6(a)) are predicted only if the frozen ground beneath the snow is assumed to have a substrate. The wave speeds and densities in the frozen ground and the substrate have been chosen to have reasonable values and to match the measured arrival time of the precursor. The assumed thickness of the frozen ground layer has been varied for best fit.

There is a clear secondary arrival and a significant precursor in the measured radial seismic component. However these measured precursors in the radial seismic component data are predicted only if the geophone is assumed to be at 14cm depth or less i.e. within the snow layer. The values listed in Table 2 have been used to obtain the predictions of the main and secondary arrivals in the radial seismic component shown in Figure 7(b). However, the predicted and measureed precursors coincide (Figure 7(a)), only if the compressional wave speed in the substrate is assumed to be 490 m/s (rather than the value of 690 m/s listed in Table 2).

Table 2. Ground parameter values used for snow cover predictions (Figs. 6, 7)

Parameter	1^{st} snow layer (Crust)	2^{nd} snow layer	Frozen soil layer	Unfrozen substrate
flow resistivity (σ, kPa s m^{-2})	16	4	3000	3000
Porosity (Ω)	0.7	0.8	0.27	0.27
Pore shape factor (s_p)	0.6	0.8	0.72	0.72
Grain shape factor (n')	0.5	0.5	0.5	0.5
density (ρ, kg m^{-3})	330	130	2000	1700
Layer thickness (m)	0.02	0.13	0.2	∞
P-wave speed (ms^{-1})	410	230	1900	690
S-wave speed (ms^{-1})	280	160	1000	244.5
Wave attenuation constant (α)	0.007	0.007	0.01	0.007

Source: [7]

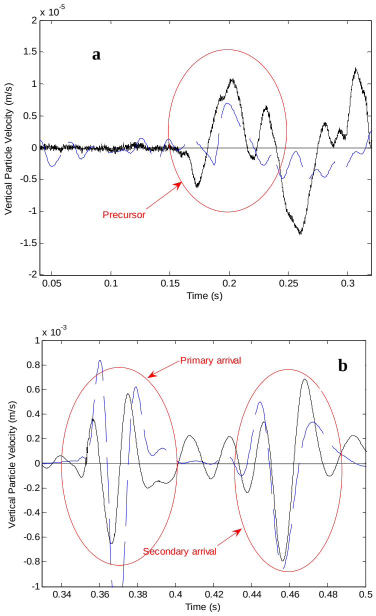

Source: [7]

Figure 6. Measured (solid lines) and predicted (broken lines) vertical component seismic signals at a snow-covered site: (a) precursor and (b) main and secondary arrivals (note different y-axis scales). Parameters used for predictions are in Table 2.

The agreement of predicted with measured time of the secondary arrival in Figure 6(b) can be improved by assuming a shear wave speed of 249 m/s for the substrate (instead of 244.5 m/s). However this adjustment would reduce the relatively good agreement obtained for the vertical component (Figure 6(a)). The high frequency jitter in the main and secondary arrivals in the radial component signal (Figure 7) (more pronounced in Figure 7(b) partly as a result of the different vertical scale) may be due to sensor resonance. However they are predicted to some extent if the radial component sensor is assumed to be inside the snow layer.

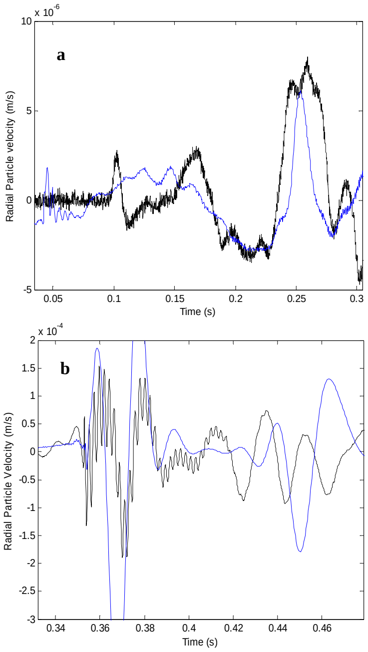

Figure 7. Measured (black lines) and predicted (blue lines) radial component seismic signals at a snow-covered site: (a) precursors and (b) main and secondary arrivals.

ACOUSTIC-SEISMIC COUPLING SPECTRA

The ratio of the vertical particle velocity of the soil as a function of frequency at a point, measured with a surface-mounted geophone, to the pressure measured by a (collocated) microphone immediately above the geophone yields the acoustic-to-seismic coupling (A/S) spectrum.

Figure 8 shows examples of measured acoustic-to-seismic coupling spectra obtained by transmitting continuous sound from a loudspeaker source to geophones buried in (a) quarry sand and (b) a dry layered soil [10]. The acoustic-to-seismic coupling spectra and pulse waveforms are influenced strongly by discontinuities in the elastic wave properties. At frequencies corresponding to peaks in the A/S spectrum, there are local maxima in the transfer of sound energy into the soil [11]. These are associated with constructive interference between transmitted and returning waves within each soil layer. Consequently, there is a relationship between near-surface layering in soil and the peaks or 'layer resonances' that appear in the measured A/S spectrum: the lower the frequency of the peak in the spectrum, the deeper the associated layer. Straightforward tracking of the frequencies of these peaks for different measurement positions has been proposed for deducing the presence and uniformity (or thickness) of soil layering [9].

Figure 8 also shows predictions using FFLAGS. In this case, the fitting procedure has made use of the predicted frequency dependence of deduced surface admittance and phase speed and measurements of slow wave phase speed and attenuation made with buried probe microphones [10] to deduce values of the pore-related parameters or of ratios of them. For example the high frequency limits of surface impedance and phase speed are predicted to be (tortuosity/porosity) and (sound speed in air/tortuosity) respectively; while the low frequency limits depend on air permeability. Subsequently these values have been used together with 'approximate' layer depths and wave speeds based on shallow seismic refraction surveys to fit data for the acoustic-to-seismic coupling spectra at the surface. This procedure yields refined values for layer depths and wave speeds (hence density and elastic moduli). The steps were repeated iteratively to achieve 'best fit' values.

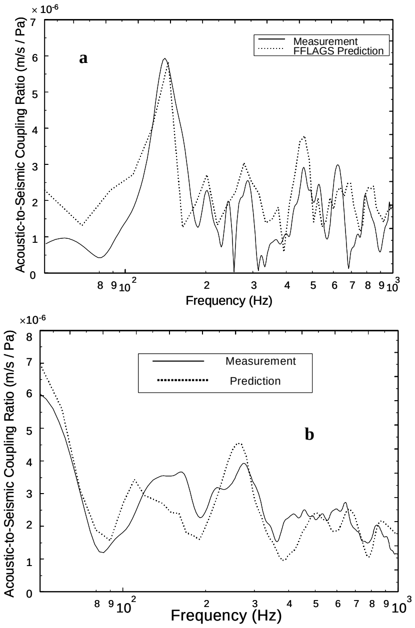

Source: [10]

Figure 8. Measured and predicted spectra of the acoustic-to-seismic coupling ratio (a) for quarried sand (range 3.0m, source height 0.75 m) consisting of two layers of similar density (1500 kg m^{-3}), permeability (5×10^{-6} m^2) and thickness (0.9 m) but different wave speeds (i.e. elastic constants) above a denser (2000 kg m^{-3}), less permeable (5×10^{-8} m^2) substrate; (b) for dry layered soil (source height 0.45 m, range 3 m) consisting of two layers (0.55m and 1.5 m thick) with similar densities (2000 and 2200 kg m^{3}) and permeabilities (approximately 5×10^{-6} m^2) but different wave speeds, above a denser (2000 kg m^{-3}) less permeable (5×10^{-8} m^2) substrate.

Characterisation of the acoustical properties of poroelastic media using Biot theory requires at least eight physical parameters in each distinct layer [1]. But a conjunctive use of acoustic and seismic measurements obtained from probe microphones and geophones, respectively, has yielded values of several parameters in reasonable agreement with non-acoustically-measured values for sand (within 20%) [10]. In the case of friable soil the agreement between acoustically-deduced parameter values with non-acoustically-measured data is less good (within 50%). On the other hand conventional non-acoustical measurements were extremely difficult for this soil [10]. Moreover by fitting the spectra with FFLAGS it was possible to distinguish differences in the air-filled porosity of adjacent soil plots (0.18 and 0.12).

PROSPECTS FOR NON-INVASIVE ACOUSTIC-SEISMIC MONITORING OF SOILS

A method for non-invasive sensing of soil structure and the mechanical strength of soil would permit better decisions about appropriate soil management practices. The numerical code and fitting procedures described in this paper have shown that conjunctive use of data for above- and below-ground propagation from impulsive acoustical excitation of soils can be used to deduce pore- and elasticity-related parameters of soils and could be the basis for a non-invasive acoustic-seismic method for sensing soil structure, strength and moisture content. Moreover it has been demonstrated that the P-wave velocity in soil is highly correlated with the internal stress in a soil [12, 13, 14]. This suggests that P-wave velocities determined remotely from non-invasive acoustic-seismic probing could be used to measure mechanical stress in soil and hence its resistance to root elongation. Furthermore measurements in the laboratory and in instrumented pits outdoors have shown that the velocity and attenuation of sound in soil are related to soil density, water content, matric potential and porosity [15].

To provide the basis for *in situ* non-invasive monitoring of surface air permeability and layering, it will be important to investigate the possibility of supplementing acoustic-to-seismic coupling data with acoustic *reflection* measurements instead of making probe microphone (transmission) measurements and conducting a conventional seismic refraction survey. Use of sound reflection, i.e. complex surface impedance data, should avoid some of the problems that arise with probe microphone measurements in loose soils and in high flow resistivity soils where the type II (mainly pore-borne) wave is attenuated too rapidly with depth. As a function of frequency, acoustical reflection measurements area-average effects of surface roughness. Also it will be important to assess the accuracy and reliability of non-contact alternatives to geophone measurements of surface soil particle velocity. Non-contact measurements of particle velocity will avoid many of the problems resulting from poor and variable geophone coupling to soil [10]. Scanning Laser-Doppler Velocimeter (LDV) measurements of acoustically-induced soil particle velocity are used routinely in a method for detecting buried landmines [16]. Although non-contact scanning of soil particle motion is possible also using relatively cheap ultrasonic sensors [17], ultrasonic sensors are less sensitive and strongly influenced by atmospheric turbulence [17].

Seismic coupling from acoustic (i.e. above surface) excitation measured by LDV scanning will be related to the elastic wave speeds and these can be used predict the internal stress in soil and water status. At high water contents (or matric potentials) the velocity of the wave that travels mainly through the soil water will be related functionally to soil water content (i.e. the porosity in a saturated soil) while for partial saturation the Type I and shear wave speeds are sensitive to soil moisture and confining pressure. For an idealised system of stacked spheres [18],

$$V_{Type\ I} \propto \left[\frac{p_e^{1/3} Z}{\rho \phi} \right]^{1/2} \tag{34}$$

where the effective stress, $p_e = p_t - Sp_c$, $p_t = \rho gh$ (g is the gravitational acceleration and h is the depth of interest) is the total stress or the overburden pressure, p_c is the capillarity pressure or water potential measured by a tensiometer or psychrometer, Z is a function of S, the degree of saturation, and $\rho = (1-\phi)\rho_s + \phi S \rho_w = \rho_b + \theta \rho_w$, ρ_s and ρ_w being densities of soil grains and water respectively, ϕ is porosity and θ is the moisture content. In consolidated soils p_t will be related to the pre-consolidation stress and will be greater than ρgh.

Time-of-flight measurements for the waves induced by impulsive acoustical excitation determined from scanning LDV measurements, by an analysis based on that used in the classical seismic refraction survey technique, could be used to infer wave speeds and hence soil properties (especially water content and elastic properties).

Implementation and validation of these ideas will require modification of PFFLAGS to include the dependence of wave speeds on moisture content, sensitivity analyses to investigate possibilities for restricting the required number of parameters and searches of parameter-space, and extensive laboratory and field trials.

ACKNOWLEDGEMENTS

The authors are grateful to Dr Patrice Boulanger for his initial work with PFFLAGS and to USACE for funding from SERDP SEED Project SI-1410.

REFERENCES

1 J.-F. Allard, *Propagation of sound in porous media* (Elsevier Applied Science, London, 1993)

2 S. Tooms, S. Taherzadeh and K. Attenborough, "Sound propagation in a refracting fluid above a layered fluid-saturated porous elastic material" *J. Acoust. Soc. Am.* **93**, 173-181 (1993)

3 M.A. Biot, "Mechanics of deformation and acoustic propagation in porous media" *J. Appl. Phys.* **33**, 1482-1498 (1962)

4 M.A. Biot, "Generalized theory of acoustic propagation in porous dissipative media" *J. Acoust. Soc. Am.* **34**, 1254-1264 (1962)

5 R. D. Stoll, "Theoretical aspects of sound transmission in sediments" *J. Acoust. Soc. Am.* **68**, 1341-1350 (1980)

6 K. Attenborough, "On the acoustic slow wave in air-filled granular media" *J. Acoust. Soc. Am.* **81**, 93-102 (1987)

7 D. Albert, K. Attenborough, S. Taherzadeh and P. Boulanger, "Ground vibrations produced by surface and near-surface explosions" paper submitted to *Applied Acoustics* (2010)

8 J. M. Sabatier, H. E. Bass, L. N. Bolen and K. Attenborough, "Acoustically induced seismic waves" *J. Acoust. Soc. Am.* **80**, 646–649 (1986)

9 W.B. Howard "An acoustic to seismic coupling survey of the fragipan horizon" MS Thesis, The University of Mississippi, USA (2002)

10 N.D. Harrop, "The exploitation of acoustic-to-seismic coupling for the determination of soil properties" Ph.D. Thesis, The Open University, UK (2000)

11 J. M. Sabatier, H. Hess, W. P. Arnott, K. Attenborough, M. J. M Romkens and E. H. Grissinger, "In situ measurements of soil physical properties by acoustical techniques" *Soil Sci. Soc. Am. J.* **54**, 658-672 (1990)

12 K. Nakagawa, K. Soga and J.K. Mitchell, "Observation of Biot compressional wave of the second kind in granular soils" *Geotechnique* **47**, 133-147 (1997)

13 K. Nakagawa, K. Soga and J.K. Mitchell, "Pulse transmission system for measuring wave propagation in soils" *Journal of Geotechnical Testing* **122**, 302-308 (1996)

14 Z. Lu, C.J. Hickey and J.M. Sabatier, "Effects of compaction on the acoustic velocity in soils" *Soil Sci. Soc. Am. J.* **68**, 7–16 (2004)

15 Z. Lu and J.M. Sabatier, "Effects of soil water potential and moisture content on sound speed" *Soil Sci. Soc. Am. J.* **73**, 1614-1625 (2009)

16 N. Xiang and J. M. Sabatier, "An experimental study on antipersonnel landmine detection using acoustic-to-seismic coupling" *J. Acoust. Soc. Am.* **113**, 1333–1341 (2003)

17 A. G. Petculescu and J. M. Sabatier "Air-coupled ultrasonic sensing of grass-covered vibrating surfaces; qualitative comparisons with laser Doppler vibrometry" *J. Acoust. Soc. Am.* **115**, 1557–1564 (2004)

18 W. Brutsaert and J. Luthin, "The velocity of sound in soils near the surface as a function of the moisture content" *J. Geophys. Res.* **69**, 643-652 (1964)